RESEARCH ARTICLE

NANO · MICRO small
www.small-journal.com

Enhanced Hot/Free Electron Effect for Photocatalytic Hydrogen Evolution Based on 3D/2D Graphene/MXene Composite

Qian Wang, Zhantong Ye, Xiaoyu Zhao, Hejing Wang, Shengyan Zhang, Suling Zhang, Hongyan Liu, Yanhong Lu, Menggai Jiao,* Yanfeng Ma, and Yongsheng Chen**

Photocatalytic hydrogen production through water splitting represents a promising strategy to store solar energy as chemical energy. Current photocatalysts primarily focus on traditional semiconductor materials, such as metal oxides, sulfides, nitrides, g-C_3N_4, etc. However, these materials often suffer from large bandgap and fast charge recombination, which limit sunlight utilization and result in unsatisfactory photon conversion efficiency. Here, a novel 3D/2D graphene/MXene (3DGraphene/MXene) photocatalyst without metal semiconductor participant is designed, and an enhanced hot/free electron catalytic mechanism for photocatalytic hydrogen evolution is proposed. The hot/free electrons, ejected out from 3DGraphene based on an Auger-like light induced electron emission mechanism and enhanced by the cocatalyst MXene $Ti_3C_2T_x$, exhibit exceptional catalytic activity under wide spectrum range from ultraviolet to visible light. The optimized 3DGraphene/MXene composite catalyst achieves an average hydrogen production rate of 1.4 mmol h^{-1} $g_{cat}{}^{-1}$. Furthermore, consistent with the proposed hot/free electron emitting mechanism, the photocurrent rises with increasing the photon energy from visible to ultraviolet light and the light intensity under the same frequency range. These results indicate that using the hot electron generated from graphene and enhanced by other 2D materials might be an effective strategy for enhancing the activity of the photocatalytic materials for water splitting.

1. Introduction

Hydrogen, as a typical green fuel and an essential material for chemical industry, holds significant importance for both renewable energy and the earth's ecosystem.[1,2] Photocatalytic water splitting for hydrogen production is one of the most important approaches to produce hydrogen from solar energy.[3–6] Photocatalysts play a pivotal role in achieving highly efficient hydrogen production. The photocatalytic process generally includes three crucial steps, incident light harvesting, charge separation/migration, and surface catalytic reduction reactions. Therefore, photocatalysts with an appropriate bandgap for full spectrum active including the visible light range, high electronic conductivity to facilitate rapid carrier transfer rates, and suitable surface environment for fast chemical reaction, are required to achieve optimal photocatalytic efficiency.[7,8]

Semiconductors, such as metal oxides,[9,10] sulfides,[11,12] nitrides,[13,14] and covalent organic frameworks,[15–17] etc., with the advantages of material diversity, structure controllability, and performance tunability, have been widely studied as the photocatalysts for hydrogen evolution through water splitting. However, the simultaneous requirements for a large bandgap, rapid charge-hole recombination rate, and limited absorption of visible-near-infrared light pose significant obstacles to the development of an efficient, practical, and renewable solar hydrogen

Q. Wang, Z. Ye, X. Zhao, S. Zhang, S. Zhang, H. Liu, Y. Lu
School of Chemistry & Material Science
Langfang Normal University
Langfang 065000, China
E-mail: yanhonglu@lfnu.edu.cn

H. Wang, M. Jiao
Interdisciplinary Research Center for Sustainable Energy Science and Engineering (IRC4SE2)
School of Chemical Engineering
Zhengzhou University
Zhengzhou 450001, China
E-mail: jiaomenggai@nankai.edu.cn

The ORCID identification number(s) for the author(s) of this article can be found under https://doi.org/10.1002/smll.202407863

DOI: 10.1002/smll.202407863

M. Jiao
School of Materials Science and Engineering
Institute of New Energy Material Chemistry
Renewable Energy Conversion and Storage Center
Key Laboratory of Advanced Energy Materials Chemistry (Ministry of Education)
Nankai University
Tianjin 300350, China

Y. Ma, Y. Chen
The Centre of Nanoscale Science and Technology and Key Laboratory of Functional Polymer Materials
State Key Laboratory and Institute of Elemento-Organic Chemistry
College of Chemistry
Nankai University
Tianjin 300071, China
E-mail: yschen99@nankai.edu.cn

production process.[18–20] Despite the improvement in hydrogen evolution efficiency achieved through tremendous studies and many pioneering works,[21–34] the practical application of these photocatalysts is hindered by their low yield, primarily attributed to the suboptimal full-spectrum utilization, especially in the visible light range and sluggish charge carrier dynamics. This limitation stems from the fact that hydrogen evolution reaction from water splitting is a thermodynamically uphill reaction that relies on the transfer of multiple electrons.[35] Therefore, to achieve efficient hydrogen production, it is highly demanded to seek alternative photocatalysts with highly energetic electrons emitting properties across a broader sunlight spectrum and rapid electron transport capabilities simultaneously.

Graphene, a novel 2D carbon material, exhibits a unique capability to reach a reverse saturation state with high density ($\approx 10^{13}$ cm^{-2})[36] of hot/free electrons well above the Fermi level. Following its distinctive Dirac band structure and an Auger-like light-induced electron emission (LIEE) mechanism, graphene can expel hot/free electrons from the Fermi level, even the Vacuum level under normal light illumination.[37,38] Exploiting this property, highly energetic hot/free electrons generated by 3D graphene (3DGraphene) have been used as the most powerful and clean reducing agents for photocatalytic ammonia synthesis directly from molecular nitrogen under mild conditions for the first time by our group.[39] Building upon this mechanism, a series of 3DGraphene based photocatalysts, integrating the intrinsic properties of 2D graphene sheets, have been developed for various photocatalytic reactions, such as hydrogen evolution from water splitting[40] and catalytic reduction of 4-nitrophenol to 4-aminophenol.[41] Benefiting from the enhanced photocatalytic abilities of the highly energetic hot/free electrons, a full-spectrum light response and improvement catalytic activities have been achieved for 3DGraphene materials. Nevertheless, their photocatalytic activity is limited by the relatively low surface chemical reaction rate due to the weak hydrophilicity of the pristine graphene sheet. Thus, we intend to introduce a cocatalyst to 3DGraphene, to provide an excellent hydrophilic surface and enhance the surface chemical reaction rate while improving the transport of high energetic hot/free electrons.

This is how MXene comes to play. MXene, a class of 2D material comprising transition metal carbides, nitrides, and carbonitrides, exhibits exceptional conductivity, superior specific surface area, tuneable terminal functional groups, hydrophilic surfaces, and favorable Gibbs free energy for hydrogen adsorption.[42–44] These unique characteristics are beneficial for promoting the separation and migration of photogenerated carriers and increasing surface active sites. Thus, these distinguished optoelectronic properties have rendered MXene to emerge as a desirable cocatalyst for hydrogen production with an obviously enhanced photocatalytic efficiency.[45–48] For example, Qiao's group conducted a pioneering work in exploring the potential role of $Ti_3C_2T_x$ as a cocatalyst for the hydrogen evolution reaction using density functional theory (DFT) calculations.[49] Also recently, Ruan et al. developed a ternary heterogeneous photocatalyst through an electrostatic self-assembly method utilizing MXene as the cocatalyst. The synergistic effect of homo-interface engineering and Ti_3C_2 MXene in the prepared composite resulted in significantly enhanced photocatalytic hydrogen evolution performance, characterized by widened light absorption and efficient carrier transportation.[50]

With these thoughts, in this study, a 3D/2D hybrid/composite (3DGraphene/MXene) has been designed by combining the advantages of 3DGraphene with efficient high energetic hot/free electrons emission properties and the superiority of 2D MXene. The composite consisted of 2D MXene ($Ti_3C_2T_x$) loaded onto 3DGraphene, and its performance in photocatalytic hydrogen evolution process from water splitting under light illumination was investigated. In this 3DGraphene/MXene composite catalyst, the 3DGraphene component serves as an electron reservoir following the LIEE mechanism even under visible light illumination. The MXene component acts as a booster/cocatalyst for facilitating the transport of generated hot/free electrons and aiding in the reduction of hydrogen on the hydrophilic surface of the composite photocatalyst. Through this synergistic design, a maximum average hydrogen production rate of 1.4 mmol h^{-1} g_{cat}^{-1} under UV-visible light was obtained.

2. Results and Discussion

2.1. Materials, Morphology and Structural Properties

2D $Ti_3C_2T_x$ and graphene oxide (GO) were prepared through exfoliation of the Ti_3AlC_2 phase by LiF/HCl[51] and the modified Hummer's method,[38,39] respectively. The bulk 3DGraphene/MXene composite material, which involved loading 2D $Ti_3C_2T_x$ sheets onto bulk 3D cross-linked graphene materials,[38–41] was prepared by using the 2D GO and $Ti_3C_2T_x$ materials above through a simple and easily scalable hydrothermal reaction followed by a freeze drying process, as shown in **Figure 1**. It is worth noting that graphene here stands for reduced graphene oxide (rGO) as it is partially reduced during the hydrothermal process. A series of 3DGraphene/MXene composite with varying proportions of MXene with 5%, 10%, 15%, and 20% were obtained and labeled as 3DGraphene/MXene-5, 3DGraphene/MXene-10, 3DGraphene/MXene-15, and 3DGraphene/MXene-20, respectively. Additionally, using the same synthesis method as described above, the control samples, including 3DGraphene without MXene and Con-MXene without graphene, were also synthesized for the comparison.

X-ray diffraction (XRD) characterization was carried out to study the phase and crystal structure of the prepared pristine MXene and 3DGraphene/MXene composite. In **Figure 2a**, the diffraction peak of Ti_3AlC_2 at $2\theta = 39.02°$ disappeared after etching, and the characteristic peaks at $2\theta = 6.4°$ and $2\theta = 13.5°$ being indexed to the (002) and (004) planes of the $Ti_3C_2T_x$ were shown simultaneously, indicating the removal of the interlayer Al element and the presence of 2D $Ti_3C_2T_x$.[47] In the XRD patterns of the 3DGraphene/MXene-10 composite, in addition to the broad peak $\approx 25°-30°$ belonging to the (002) plane of graphene, the diffraction peak of the (002) plane of $Ti_3C_2T_x$ at $< 10°$ was reserved, confirming successful loading of $Ti_3C_2T_x$ on 3DGraphene to form the composite. In addition, the wider diffraction peak of (002) plane and the absence of significant other peaks of $Ti_3C_2T_x$ in the 3DGraphene/MXene composite demonstrated improved dispersion and disordered stacking of $Ti_3C_2T_x$ embedded in the 3DGraphene skeleton.[52] These XRD results indicate

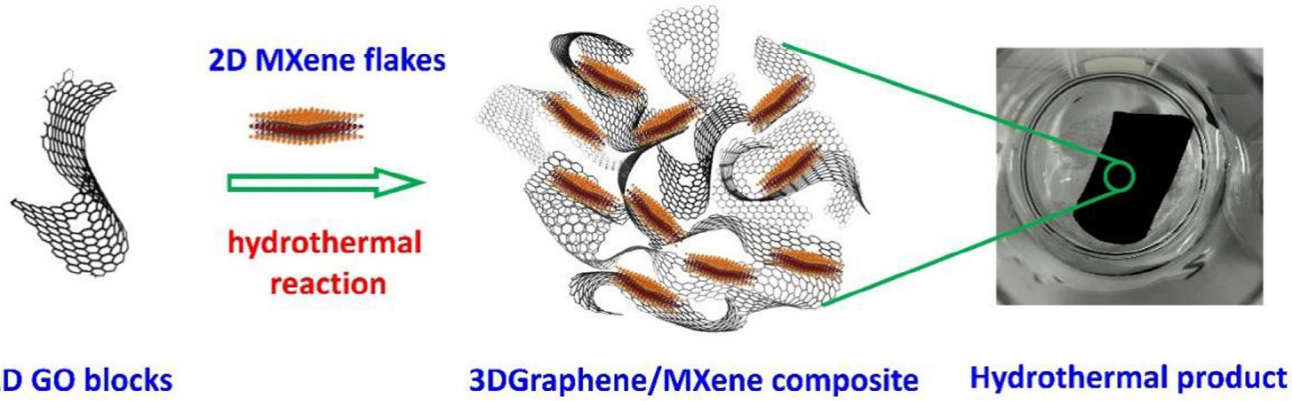

Figure 1. Schematic diagram for the synthesis of 3DGraphene/MXene composite photocatalyst. A typical digital photograph at the right is presented for the 3DGraphene/MXene product.

that $Ti_3C_2T_x$ and 3DGraphene maintain their intrinsic structure within the composites.

Raman spectra were carried out to further understand the structure of the prepared $Ti_3C_2T_x$ and 3DGraphene/MXene-10 composite, as presented in Figure 2b. The characteristic peak of $Ti_3C_2T_x$ at 204 cm^{-1} corresponds the A_{1g} symmetry out-of-plane vibrations of Ti atoms, whereas the peaks of 387 and 601 cm^{-1} arise from the E_g group vibrations, consisting of the in-plane (shear) modes of Ti, C, along with the surface functional group atoms.[52,53] In the Raman spectrum of 3DGraphene/MXene composite, all the characteristic peaks of $Ti_3C_2T_x$ in the range of 200–600 cm^{-1} are observed, indicating that the structure of $Ti_3C_2T_x$ is maintained in the composite. It is worth noting that the peaks of $Ti_3C_2T_x$ at 204, 387, and 601 cm^{-1} slightly shifted to 210, 415, and 610 cm^{-1}, respectively, after being loaded on the 3DGraphene surface, indicating the presence of hydrogen bonding and van der Waals interaction between $Ti_3C_2T_x$ and 3DGraphene. At higher wavenumber, the typical peaks of graphene, D (1347 cm^{-1}), and G (1588 cm^{-1}) bands are observed, corresponding the breathing modes of six-atom rings and the high-frequency E_{2g} phonon at the G-point, respectively.[53]

The chemical composition and surface electronic states of the 3DGraphene/MXene composite and the control sample of $Ti_3C_2T_x$ were employed by X-ray photoelectron spectroscopy (XPS) characterization. The XPS survey spectra are shown in Figure 2c, where the peaks of C 1s, Ti 2s, Ti 2p, and O 1s appear in both $Ti_3C_2T_x$ and 3DGraphene/MXene-10 composite, demonstrating the formation of the composite. The high-resolution XPS spectra of Ti 2p and C 1s provide the detailed electronic states of the two samples, as shown in Figure 2d,e. In the fitting peaks of Ti 2p of $Ti_3C_2T_x$, the Ti $2p_{3/2}$ components centered at 455.3, 456.3, and 458.0 eV can be assigned to Ti—C, Ti (II) and Ti—O bonds of Ti $2p_{3/2}$, respectively. The Ti $2p_{1/2}$ component located at 461.7 and 464.9 eV corresponds to Ti—C and Ti—O.[54] In the high-resolution Ti 2p spectra of 3DGraphene/MXene-10 composite, the Ti—C $2p_{1/2}$ component located at 463.2 eV of the $Ti_3C_2T_x$ is retained. Meanwhile, the intensity of Ti—O $2p_{3/2}$ and Ti—O $2p_{1/2}$ components located at 459.7 and 465.4 eV is obviously enhanced, indicating the interaction force between 3DGraphene and $Ti_3C_2T_x$. The high-resolution C 1s spectra of $Ti_3C_2T_x$ are fitted with three main components, 281.2, 284.4, and 285.4 eV, being assigned to Ti—C, C—C, and C—O bonds, respectively. For 3DGraphene/MXene-10 composite, the peaks of C—C, C—O and O—C=O bonds are observed at 284.0, 285.3, and 286.5 eV, respectively, representing the typical electron states of 3DGraphene. No obvious Ti—C peak was found in the composite, caused likely by the relatively low mass content and high embedding in the 3DGraphene bulk skeleton. To confirm the surface terminations of the $Ti_3C_2T_x$, the high-resolution spectrum in the O 1s region was studied, as shown in Figure 2f, which could be assigned to three components at 530.3, 531.7, and 533.2 eV, respectively. The peaks of 530.3 and 531.7 eV can be attributed to the oxygen in Ti—O and —OH groups,[55] while the component at 533.2 eV likely arises from the absorbed water. Fourier-Transform Infrared (FT-IR) spectrum was further performed (Figure 2g). The adsorption peaks at 3436, 2929, and 1646 cm^{-1} could be assigned to the asymmetric stretch of −OH, asymmetric vibration of −OH, and bending vibration of −OH, respectively.[56] The presence of Ti—C and Ti—O bonds in the high-resolution spectra of Ti 2p and O 1s, in conjunction with the FT-IR result, demonstrates the presence of —OH termination in $Ti_3C_2T_x$, indicating the formation of $Ti_3C_2(OH)_2$.[51]

The morphology of the composite, which depends on the structure of precursors and the synthesis process, plays a crucial role in determining the photocatalytic activity. This morphology was characterized using a scanning electron microscope (SEM). The prepared $Ti_3C_2T_x$ has a 2D layered structure, as shown in the SEM image in **Figure 3a**. By optimizing the hydrothermal process, a cross-linked 3DGraphene was obtained to serve as the skeleton in the 3DGraphene/MXene composite. Figure 3b,c depict the framework of 3DGraphene/MXene-10 composite, consisting of 2D flexible graphene sheets as the units, where 2D $Ti_3C_2T_x$ sheets attach on by probably face-to-face based on the hydrogen bonding and the van der Waals interaction. Transmission electron microscope (TEM) was further performed for the morphology analysis of the photocatalysts. Figure 3d shows the 2D sheet of the prepared $Ti_3C_2T_x$, consistent with the SEM results. From the TEM image (Figure 3e) of the 3DGraphene/MXene-10 composite, the $Ti_3C_2T_x$ layers (signed with the white dotted circles) loaded on the surface of graphene sheets were observed. Figure 3f–i presents the energy dispersive spectroscopy (EDS) images, illuminating the

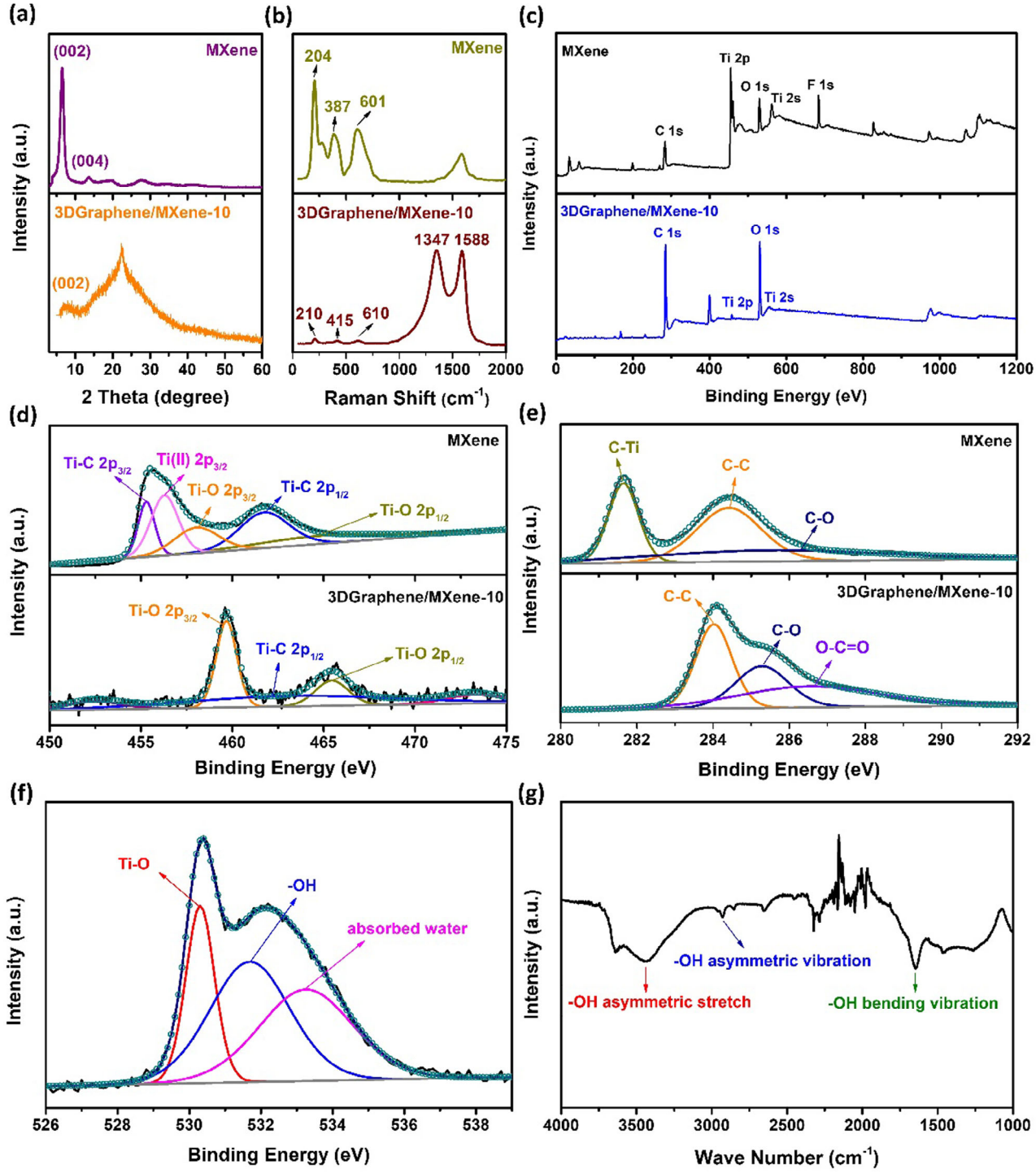

Figure 2. Structure analyses of the prepared $Ti_3C_2T_x$ and 3DGraphene/MXene-10 composite. a) X-ray diffraction spectra. b) Raman spectra. c) XPS survey spectra. d) high-resolution Ti 2p spectra. e) high-resolution C 1s spectra. f) high-resolution O 1s spectrum of MXene. g) FT-IR spectrum of $Ti_3C_2T_x$.

formation of the composites, with even distribution of Ti element (MXene) as expected. The morphology analysis of the 3DGraphene/MXene composite reveals that 3DGraphene retains the individual 2D graphene sheet structure, thereby maintaining the unique and remarkable mechanical and (opto)electronic properties of graphene. 2D $Ti_3C_2T_x$ layers, closely adsorbing on the surface of graphene sheets, can benefit to the transportation of the high energetic free/hot electrons emitting from the graphene sheets, enhancing the photocatalytic properties of the composite.

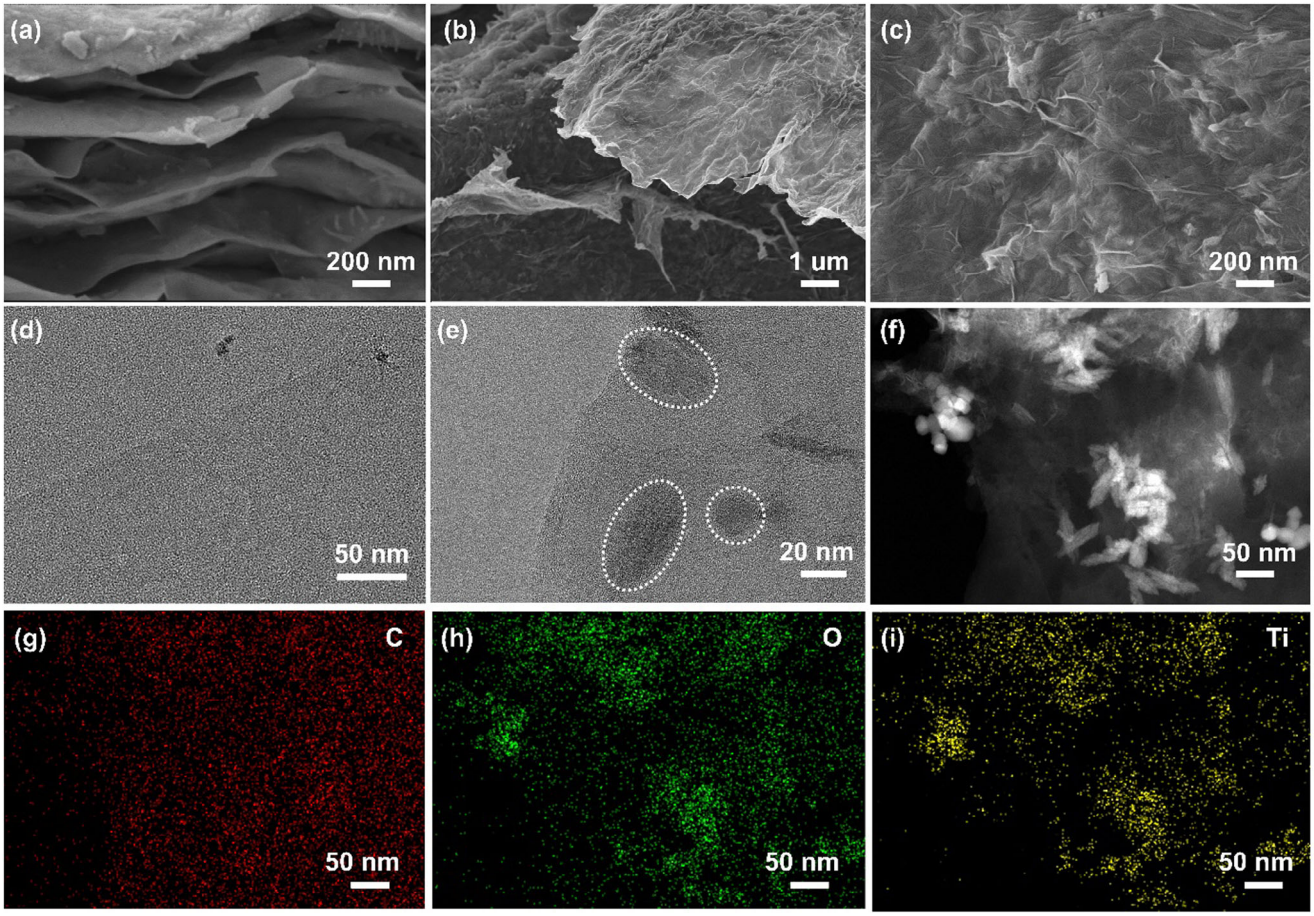

Figure 3. SEM images of a) cross section of $Ti_3C_2T_x$ film, and b) low-, c) high-magnification of 3DGraphene/MXene-10 composite. TEM images of d) $Ti_3C_2T_x$ and e) 3DGraphene/MXene-10 composite. f–i) EDS images of 3DGraphene/MXene-10 composite.

2.2. Light-Harvesting and Photoelectrochemical Properties

The light-harvesting capability of 3DGraphene and 3DGraphene/MXene composite was evaluated by the ultraviolet-visible DRS. As shown in **Figure** 4a, it can be observed that MXene exhibits strong absorption in the visible light region. Both 3DGraphene and 3DGraphene/MXene composite show excellent absorption across the full ultraviolet-visible spectrum. In the visible light range, the 3DGraphene/MXene composite shows higher absorption ability compared to 3DGraphene alone, attributed to the enhanced light absorption capability of MXene. To confirm the hot/free electron enhancement effect of MXene and its role in charge separation in the 3DGraphene/MXene photocatalyst, photoluminescence (PL) measurements were conducted, as shown in Figure 4b. The 3DGraphene/MXene composite exhibited lower intensity than 3DGraphene, demonstrating the enhanced effect of MXene in facilitating the rapid transmission of emitting hot/free elections and their separation from the photoinduced holes.[47] The electrochemical impedance spectroscopy (EIS) measurements were further performed to clarify the electron transfer kinetics. In Figure 4c, the Nyquist plots of 3DGraphene, Con-MXene, and 3DGraphene/MXene-10 materials exhibit similar characteristics, with a typical semicircle and an inclined line in the low and high-medium frequency region, respectively. The Con-MXene sample shows the smallest radius semicircle, indicating the lowest interfacial charge transfer resistance and excellent electronic conductivity.[57] This suggests an enhanced charge transport capability of the composite catalyst due to the presence of the cocatalyst MXene, aligning with the design strategy. According to the DRS and PL results, the introduction of MXene into the composite enhances the electron separation and transfer ability of the 3DGraphene/MXene-10 materials compared with the control 3DGraphene material, which is indicative of a faster electron transportation process during photocatalytic hydrogen evolution process. The transient photocurrent measurements were further carried out. As shown in Figure 4d, the photocurrent response signals of the 3DGrahpene and 3DGraphene/MXene photocatalysts were measured, which identify its available photogenerated hot/free electron property under both the ultraviolet and visible light irradiation. For the control sample of Con-MXene, no detectable or negligible photocurrent signal was detected. Compared with the 3DGraphene alone, the 3DGraphene/MXene-10 composites exhibited higher photocurrent intensity under both ultraviolet and visible light illumination, which can be ascribed to the enhanced effect of the MXene cocatalyst. Additionally, the enhanced photocurrent intensity with increasing light power under ultraviolet light illumination for both 3DGraphene/MXene-10

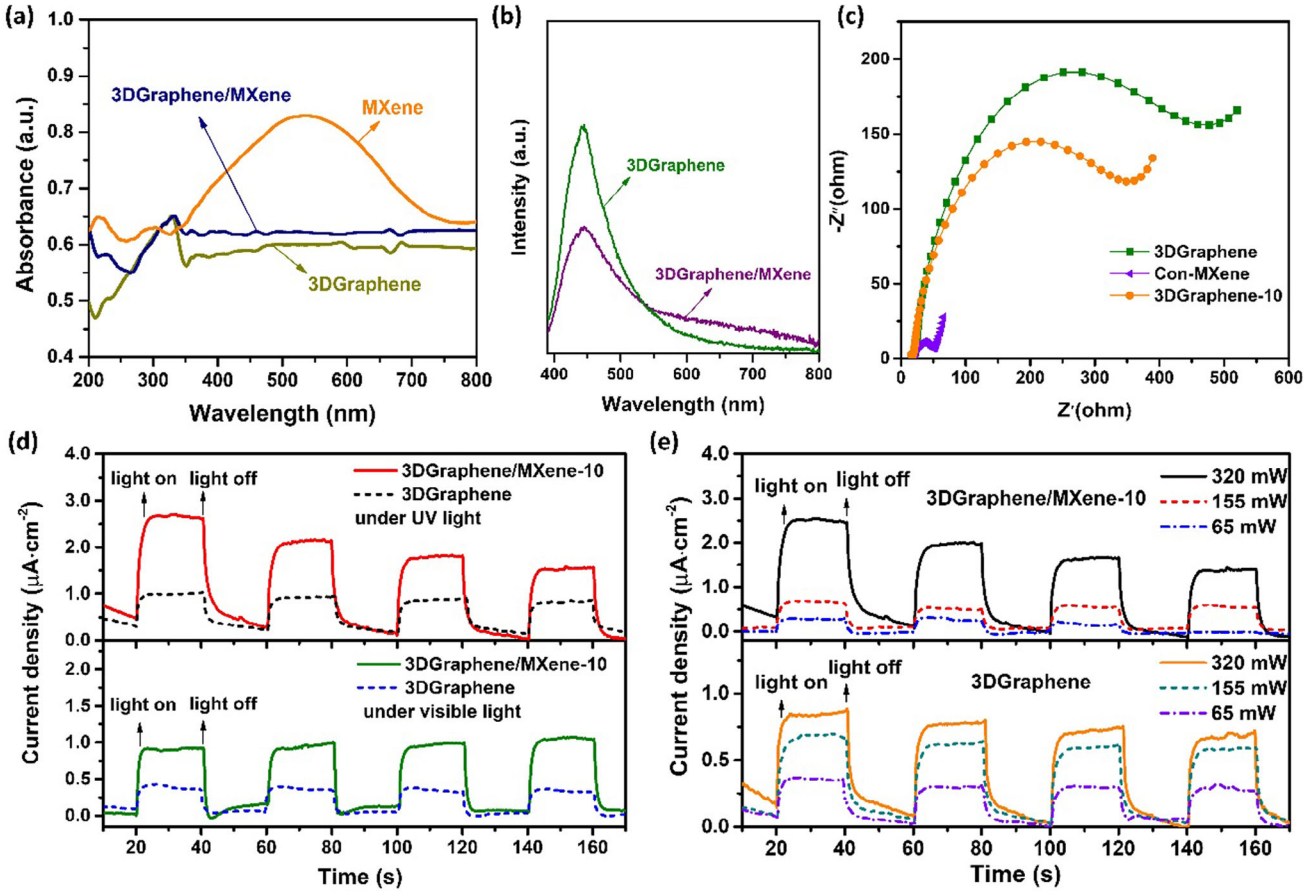

Figure 4. a) ultraviolet-visible diffuse reflectance spectra and b) photoluminescence spectra of 3DGraphene and 3DGraphene/MXene. c) Nyquist plots of the 3DGraphene/MXene-10 photocatalyst and the control samples of 3DGraphene and Con-MXene. d) transient photocurrent of the 3DGraphene/MXene-10 and 3DGraphene under ultraviolet and visible light ($\lambda > 420$ nm) respectively, the light was turned on/off every 20 s. e) transient photocurrent of the 3DGraphene/MXene-10 and 3DGraphene under ultraviolet light illumination with different irradiation power density of 427, 207, and 87 mW cm^{-2}, respectively.

and 3DGraphene photocatalysts (Figure 4e) further illustrates the hot/free electron emitting properties of these photocatalyst.

2.3. Photocatalytic Hydrogen Evolution

The photocatalytic hydrogen evolution reaction through water splitting under light illumination and the photocatalytic activities of 3DGraphene/MXene along with that of the control photocatalysts were assessed following the standard procedure using an on-line photocatalytic reaction system equipped with gas chromatograph. As shown in **Figure** 5a, almost no hydrogen evolved for the control Con-MXene sample, indicating that bare MXene material does not exhibit photocatalytic activity. In contrast, the control sample pristine 3DGraphene exhibits catalytic activity under the light irradiation, consistent with our earlier reported results,[39–41] and further confirming the catalytic ability of the generated hot/free electrons. As expected, upon employing the 3DGraphene/MXene photocatalyst, a dramatically enhanced hydrogen evolution rate was achieved, as indicated with increased photocurrent signals shown in Figure 4d.

The amount of hydrogen production based on the 3DGraphene/MXene photocatalyst was observed to increase with increasing ratio of MXene cocatalyst in the composite, reaching a maximum of 3657 μmol g_{cat}^{-1} during the first 4 h of the reaction for the 3DGraphene/MXene-10 photocatalyst. However, as the mass ratio of the MXene cocatalyst in the 3DGraphene/MXene composite increased further, the hydrogen evolution performance decreased. As discussed in the following photocatalytic mechanism, the synergetic effect between graphene and MXene renders the enhanced photocatalytic performance compared with both individual components and other materials reported in the literatures. The superior catalytic activity of the 3DGraphene/MXene composites can be attributed to the optimal balance between sufficient light absorption from 3DGraphene and rapid electron transfer enhanced by MXene. With increasing MXene content in the composite, excessive MXene cocatalyst aggregates on 3DGraphene surfaces will block the incident light.[47] This shielding effect reduces light absorption by the 3DGraphene matrix. While the overall light absorption by graphene decreases with MXene loading, the co-catalytic enhancement of rapid electron transfer based on

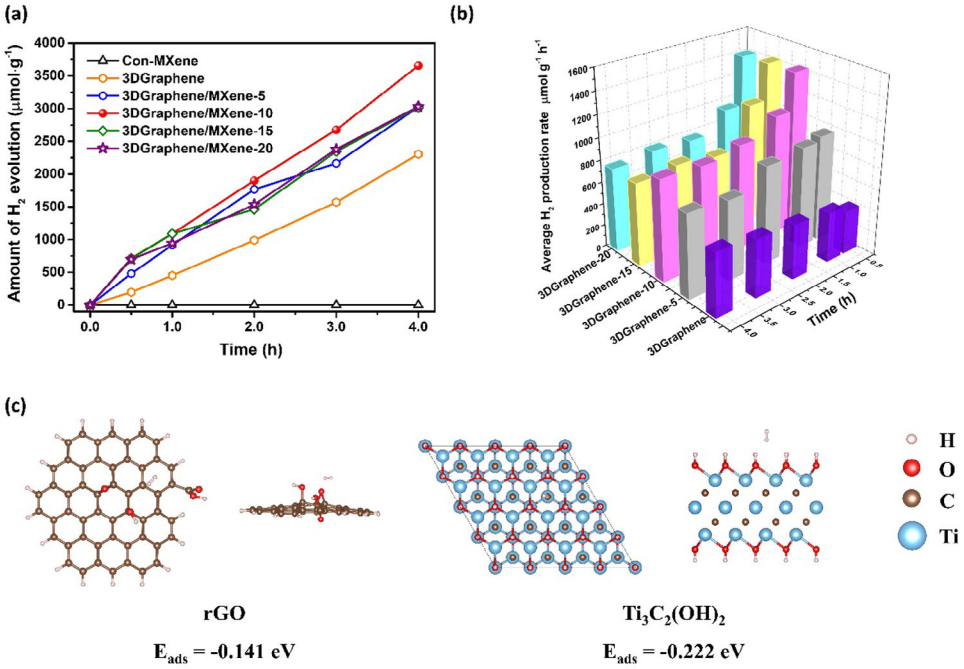

Figure 5. Photocatalytic hydrogen evolution activities and the proposed photocatalytic mechanism based on 3DGraphene/MXene photocatalysts. a) hydrogen evolution amount in 4 h and b) average hydrogen production rate at the different time on the series of 3DGraphene/MXene photocatalysts and the control samples of 3DGraphene and Con-MXene under 300 W Xe lamp illumination. c) the optimized structures and the corresponding adsorption energies of the H_2 on rGO (3DGraphene) and $Ti_3C_2(OH)_2$ surface, respectively.

MXene increases correspondingly. These competing factors reach an optimal equilibrium at 10% MXene content, achieving a hydrogen production rate of 3657 μmol g_{cat}^{-1} during the initial 4 h period.

The effect of the mass of the photocatalyst on hydrogen production performance was also studied. As shown in Figure S1 (Supporting Information), the maximum hydrogen production amount was obtained when the catalyst mass was 2 mg in 100 mL reaction solution. Due to the very low density of the material, the volume of 3DGraphene/MXene will increase greatly with the increase of the weight (Figure S2, Supporting Information). Consequently, a further increase in the dosage of the photocatalyst leads to the deterioration of the photocatalytic performance, attributing to the light shielding effect of the dark 3DGraphene/MXene composite.

The hydrogen evolution rate over different time intervals was investigated to gain a deeper understanding of the photocatalytic process. As displayed in Figure 5b, compared with the control 3DGraphene photocatalyst, all the 3DGraphene/MXene composite exhibit a higher average hydrogen production rate, while it decreased with the increase of reaction time. This trend may be inferred as that the increasing produced hydrogen molecules at the cocatalyst surface cannot be desorbed rapidly and potentially occupy active reactive sites, leading to the lower reaction rate with the reaction going on for a long time. To confirm this inference, the adsorption energy (E_{ads}) of H_2 on rGO (surface of 3DGraphene) and $Ti_3C_2(OH)_2$ was calculated using density functional theory (DFT) method. As illustrated in Figure 5c, $Ti_3C_2(OH)_2$ exhibit lower E_{ads} values of −0.222 eV than that of 3DGraphene surface with −0.141 eV, indicating a stronger binding of H_2 on $Ti_3C_2(OH)_2$ substrates, which is not favorable for the desorption of the produced H_2 desorption from the photocatalyst surface. The optimal added mass of MXene cocatalyst was found to be around 10%, with the 3DGraphene/MXene-10 composite exhibiting the highest average rates of hydrogen production, reaching 1427 and 914 μmol h^{-1} g_{cat}^{-1} in the first 0.5 and 4 h, respectively. These values are notably higher than those of 3DGraphene alone (392 and 576 μmol h^{-1} g_{cat}^{-1}) and the other 3DGraphene/MXene photocatalysts, as well as the previously reported data (**Table 1**).

The stability investigation of the 3DGraphene/MXene-10 was carried out for 5 cycles with sustaining 4 h for each cycle test (**Figure 6a**). A slight damping of the hydrogen evolution amount was observed over the cycles. To investigate the factors contributing to the reduced photocatalytic activity, the morphology and chemical states of the 3DGraphene/MXene composites after reaction for 5 cycles were examined. In the high-resolution O 1s spectrum of the fresh 3DGraphene/MXene-10 (Figure 6b), the dominant component observed was —OH. After photocatalytic reaction for 5 cycles of total 20 h, the peak of Ti—O bond at 531.5 eV became stronger, indicating the change in the surface chemical state during light illumination. Despite this change, the SEM result (Figure 6c) revealed no significant change in the overall morphology of the photocatalyst. This suggests that the 3D structure of the photocatalyst remained unchanged after the photocatalytic cycle reactions, contributing to the sustained high activity of the 3DGraphene/MXene composites. As a result, the hydrogen evolution efficiency with 71% was kept after 5 cycles, indicating a favourable cycling stability of the photocatalyst.

Table 1. Comparison of the hydrogen evolution rate for 3DGraphene/MXene with the conventional semiconductor with MXene cocatalysts.

Catalyst	Light source	H_2 evolution rate [μmol h^{-1} g_{cat}^{-1}]	Irradiation power density [mW cm^{-2}]	Specific catalytic activity [μmol h^{-1} g_{cat}^{-1} [mW cm^{-2}]$^{-1}$]	Refs.
3DGraphene/MXene	**300 W Xe lamp**	**1427**	**347**	**4.11**	**This work**
g-C_3N_4/$Ti_3C_2T_x$	350 W Xe lamp ($\lambda \geq$400 nm)	88	–	–	[58]
g-C_3N_4/$Ti_3C_2T_x$/Pt	300 W Xe lamp (λ > 420 nm)	534	150	3.56	[59]
TiO_2/$Ti_3C_2T_x$/Cu	300 W Xe lamp	860	–	–	[60]
TiO_2/$Ti_3C_2T_x$ /Ru	300 W Xe lamp (350 < λ < 780 nm)	235	–	–	[61]
g-C_3N_4/$Ti_3C_2T_x$	300 W Xe lamp (λ > 420 nm)	727	–	–	[62]
TiO_2/$Ti_3C_2T_x$	350 W Xe lamp	127	80	1.56	[63]
CdS/$Ti_3C_2T_x$	Xe lamp (λ > 420 nm)	825	–	–	[64]
g-C_3N_4/$Ti_3C_2T_x$	300 W Xe lamp	565	–	–	[65]
UiO-66-NH_2/$Ti_3C_2T_x$	350 W Xe lamp	204	–	–	[66]
CdS/$Ti_3C_2T_x$	300 W Xe lamp (λ > 420 nm)	193	750	0.26	[67]
CdS/CoO/$Ti_3C_2T_x$	300 W Xe lamp (λ > 420 nm)	134	–	–	[68]
P/TiO_2/$Ti_3C_2T_x$	300 W Xe lamp (λ > 420 nm)	684	–	–	[69]
TiO_2-COSx/$Ti_3C_2T_x$	300 W Xe lamp	950	–	–	[70]
TiO_2/$Ti_3C_2T_x$	300 W Xe lamp	783	–	–	[71]
ZnS/$Ti_3C_2T_x$	300 W Xe lamp	503	–	–	[72]
g-C_3N_4/$Ti_3C_2T_x$/Pt	300 W Xe lamp	983	–	–	[73]
$SnNb_2O_6$/$Ti_3C_2T_x$/Pt	300 W Xe lamp (λ > 420 nm)	44	–	–	[74]
g-C_3N_4/$Ti_3C_2T_x$	Solar simulator (AM1.5)	950	–	–	[75]

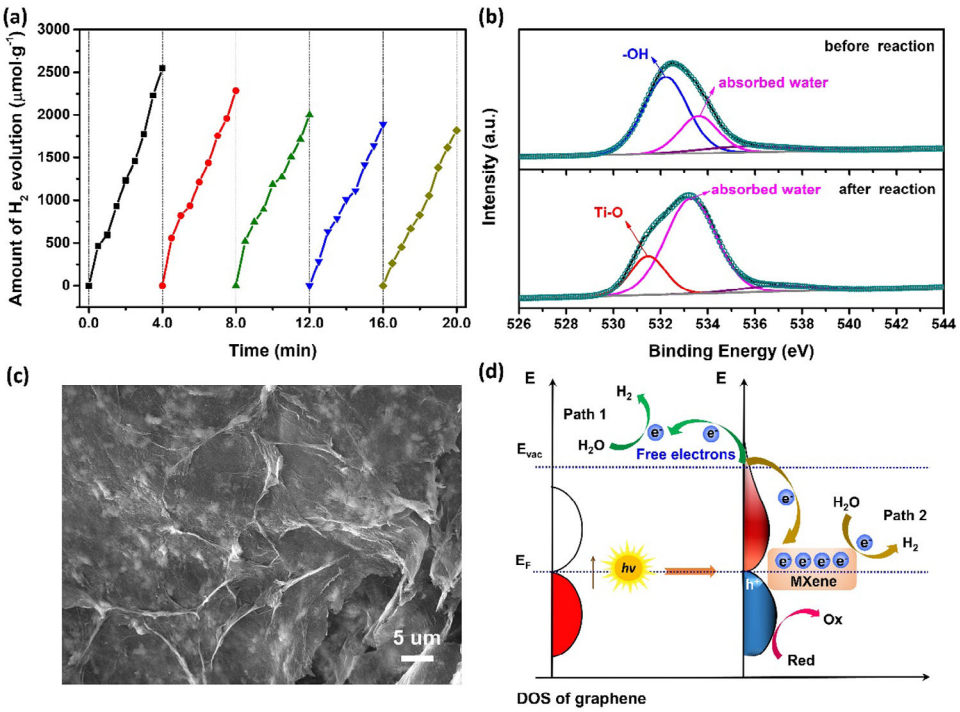

Figure 6. Stability of photocatalytic hydrogen production over 3DGraphene/MXene-10 photocatalyst under 300 W Xe lamp illumination. The reaction was continued for 20 h, every 4 h, the reaction system was purged with Ar for 30 min to remove the produced hydrogen. b) high-resolution O 1s spectra before and after and c) SEM image after photocatalytic reaction for 5 cycles of 3DGraphene/MXene-10. d) the proposed electron transfer pathways and the photocatalytic mechanism for hydrogen production on the 3DGraphene/MXene photocatalyst.

Table 2. The average hydrogen evolution rate in the first 0.5 h for 3DGraphene and series of 3DGraphene/MXene composite.

Catalyst	3DGraphene	3DGraphene/MXene-5	3DGraphene/MXene-10	3DGraphene/MXene-15	3DGraphene/MXene-20
Hydrogen evolution rate [μmol h^{-1} g_{cat}^{-1}]	392	957	1427	1418	1397

2.4. Mechanism Analysis

Based on above experimental data and discussions, a hot/free electron enhanced photocatalytic mechanism based on the 3D/2D graphene/MXene photocatalyst for hydrogen evolution is proposed, as illustrated in Figure 6d. Under light illumination, the electrons are initially produced on the surface of 3DGraphene and ejected out above the Vacuum level to free space based on its unique Dirac band structure via an Auger-like LIEE mechanism.[37,38] Acting as clean and powerful reducing agents, these highly energetic hot/free electrons can reduce water and produce hydrogen.[40] Meanwhile, the induced potential on graphene could be consumed by the methanol sacrificing agent.[39] Depending on the pathway of the electron transportation, two possible pathways for the hydrogen production are proposed. Path 1 involves the direct reduction of water to hydrogen by the photoinduced hot/free electrons on the 3DGraphene surface. Alternatively, the photogenerated hot/free electrons can efficiently transfer from the 3DGraphene to the $Ti_3C_2T_x$ surface because of the distinguished charge transfer ability of $Ti_3C_2T_x$ and the direct face-to-face contact between the $Ti_3C_2T_x$ and graphene sheets. This allows for the accumulation of hot/free electrons on the $Ti_3C_2T_x$ surface, where they can participate in the reduction of water to hydrogen, providing abundantly hydrophilic active sites for hydrogen production (Path 2). Based on the two possible pathways for the hot/free electron transfer mechanism, the synergetic effects of the MXene cocatalyst are proposed to enhance the electron transfer in the process, leading to the significantly improved hydrogen production activity of the 3DGraphene/MXene composite, surpassing conventional semiconductor with MXene cocatalysts (Table 1) and both the control samples of 3DGraphene and Con-MXene. To identify the dominant reaction path, the analysis for the hydrogen evolution rate was conducted. Considering the effect of the stability the photocatalyst, the average hydrogen evolution rate in the first 0.5 h for 3DGraphene and series of 3DGraphene/MXene composite was selected. As displayed in **Table 2**, the average hydrogen evolution rate of all 3DGraphene/MXene composite increased by more than 1 time, with the highest value reaching 3.6 times that of 3DGraphene/MXene-10 compared to 3DGraphene. Based on these findings, it can be inferred that the hot/free enhance path by MXene (Path 2) provide the dominant contribution for the hydrogen production.

3. Conclusion

In conclusion, a novel and unconventional 3DGraphene/MXene water-splitting photocatalyst, without the participation of traditional semiconductors, was designed and investigated. This photocatalyst demonstrated significantly enhanced catalytic performance following a hot/free electron catalytic mechanism due to the unique Dirac band structure and an Auger-like LIEE mechanism of 3DGraphene. A maximum average hydrogen production rate of 1.4 mmol h^{-1} g_{cat}^{-1} for the optimized 3DGraphene/MXene composite was obtained. The outstanding photocatalytic performance of the unconventional 3DGraphene/MXene composite can be ascribed to the highly synergistic effect of the excellent capability to generate high energetic hot/free electrons from 3DGraphene component and the quickly electron transfer ability and plentiful surface increased active sites of the $Ti_3C_2T_x$ component in the composite. These findings, based on the unique 3D/2D graphene/MXene photocatalyst, are expected to open up a new avenue to develop new and effective catalysts utilizing graphene and other 2D material for the efficient absorption and conversion of solar energy.

4. Experimental Section

Synthesis of 3DGraphene/MXene: GO and $Ti_3C_2T_x$ was first synthesized followed by the published works. GO was prepared through the oxidation of natural flake graphite using modified Hummers' method.[38,39] The synthesis procedure of $Ti_3C_2T_x$ was similar to that of the typical reported method of Yury's group.[76] Typically, LiF (1.6 g) was dissolved in 20 mL of 9 M HCl at room temperature under stirring for 10 min. Then, Ti_3AlC_2 powder (200 mesh, 1.0 g) was slowly added to the above LiF/HCl solution. After that, the mixture was heated to 35 °C in water bath and continuous stirring for another 24 h. The reaction suspension was subject to be centrifuged and washed thoroughly with deionized water until pH ≥ 6. The obtained suspension was then sonicated for 1 h in ice-water bath with the protection of Ar atmosphere and followed centrifuged at 3500 rpm for 1 h to remove the unetched Ti_3AlC_2, and the delaminated $Ti_3C_2T_x$ was obtained in the supernatant. For the concentration test and the SEM sample preparation, a certain amount $Ti_3C_2T_x$ solution was filtered through a PVDF membrane with 0.25 μm pore size and finally dried in vacuum oven at 60 °C for 12 h. The concentrations of the prepared GO suspension and $Ti_3C_2T_x$ solution was 8.60 and 6.57 mg mL^{-1}, respectively.

To prepare the 3DGraphene/MXene composites, GO suspension (70 mg) and a certain amount $Ti_3C_2T_x$ solution was mixed (70 mL) and stirred for 10 min at Ar atmosphere. Then, the mixture of GO and $Ti_3C_2T_x$ was sealed in a 100 mL Teflon-lined autoclave and heated up to 120 °C and maintained for 12 h. The autoclave was then naturally cooled to room temperature and the colloidal cylinder product with water (digital photograph in Figure 1) was carefully removed from the autoclave to a beaker, followed by freeze-dried process and the 3DGraphene/MXene composites were obtained finally. The prepared 3DGraphene/MXene composites with different $Ti_3C_2T_x$ added mass (5%, 10%, 15%, and 20%) are denoted as 3DGraphene/MXene-5, 3DGraphene/MXene-10, 3DGraphene/MXene-15, and 3DGraphene/MXene-20 respectively. For comparison, the control samples of 3DGraphene without MXene loading, and only $Ti_3C_2T_x$ without GO added in the hydrothermal procedure (named as Con-MXene) were synthesized through the similar process.

Catalysts Characterizations: X-ray diffraction (XRD) patterns of the catalysts were analyzed on a Bruker D8 Advance diffractometer using Cu-Kα radiation. Raman spectra were recorded using a Horiba LabRAM HR Evolution spectrophotometer with a laser of 532 nm at room temperature. X-ray photoelectron spectroscopy (XPS) was measured on an Thermo Scientific K-Alpha spectrometer equipped with a monochromatic Al Kα X-ray source ($h\nu$ = 1486.6 eV). Peak fitting was conducted using CasaXPS. Fourier-transform infrared spectroscopy (FT-IR) was investigated using a

Thermofisher Nicolet IS50 spectrometer. Scanning electron microscopy (SEM) analysis was carried out using a ZEISS Sigma 360 system with an acceleration voltage of 20.0 kV. High resolution transmission electron microscopy (HR-TEM) evaluation was performed on a FEI Talos F200X G2 with an acceleration voltage of 300 kV. Ultraviolet-visible diffuse reflectance spectrum (DRS) was measured on a Hitachi UH4150 spectrometer with an optics integrating sphere using $BaSO_4$ as the standard. Photoluminescence spectra was carried out on an Edinburgh FLS1000 fluorescence spectrometer with the excitation wavelength of 370 nm.

Photoelectrochemical Measurements: Photoelectrochemical experiments were conducted on a electrochemical workstation (Shanghai Chenhua, CHI660E) using a standard three-electrode system, where Pt wire and Ag/AgCl electrode were utilized as the counter and reference electrode respectively in a 0.2 M Na_2SO_4 aqueous solution. The working electrode was prepared by dropping the photocatalyst ink on the fluorine-doped tin oxide (FTO) conductive glass and followed by drying process. Briefly, the prepared photocatalyst (5.0 mg) was first ultrasonically dispersed for 60 min in the mixture of deionized water (735 µL), ethanol (245 µL), and Nafion (20 µL, 5 wt.% in a mixture of lower aliphatic alcohols and water, contains 45% water) solutions. Then, the prepared suspension (20 µL) was transferred onto the FTO substrate (1.0×2.0 cm^2) and subject to be dried under the infrared lamp. The transient photocurrent was performed with an applied potential of 0.35 V versus Ag/AgCl to the working electrode using a 300 W Xe arc lamp as light source. The photocurrent signals were recorded under the different irradiation power density of 427, 207, and 87 mW cm^{-2} through controlling the distance from the Xe lamp to the solution surface with 6, 26, and 46 cm, respectively. The visible light experiment was conducted under a 300 W Xe lamp equipped with an optical cutoff filter ($\lambda = 420$ nm) to eliminate the ultraviolet light. Electrochemical impedance spectroscopy (EIS) was carried out in a range of 1 Hz–100 kHz with an AC amplitude of 5 mV.

Photocatalytic Hydrogen Evolution Reaction: The photocatalytic hydrogen production test was carried out in a top-illuminated quartz vessel (250 mL) connected to an on-line photocatalytic reaction system equipped with gas chromatograph (Labsolar-4AI, Beijing Perfectlight Technology Co. Ltd.) using a 300 W Xe arc lamp (PLS-SXE) as the light source. The prepared photocatalyst (2 mg) was first dispersed with an assistant stirring into a mixed solution (100 mL) containing deionized water (90 mL) and the sacrificial reagent of methanol (10 mL). After that, the system was deaerated with ultrahigh pure Ar for 30 min to remove the dissolved oxygen. The distance from the Xe lamp to the solution surface was controlled at 8 cm and the incident light power density arrived at the liquid surface is 347 mW cm^{-2}. The photocatalytic process was proceeded under continuous stirring and the temperature of the solution was maintained at 7 °C by the circulating cooling water around the vessel. The amount of hydrogen evolved was determined via gas chromatography (Zhejiang Fuli, GC9790PLUS) equipped with a molecular sieve column and thermal conductivity detector (TCD) and argon as a carrier gas.

DFT Calculations: In this study, all DFT calculations were performed using Vienna ab-initio Simulation Package (VASP).[77] The projector augmented wave (PAW) method[78] was employed together with a plane-wave energy cutoff of 450 eV to describe core-valence electron interactions. Electronic exchange and correlation effects were delineated by the generalized gradient approximation (GGA) in the scheme of the Revised Perdew-Burke-Ernzerhof (RPBE).[79] A vacuum region of 20 Å in z direction was applied to avoid periodic boundary condition interactions between the neighboring configurations. To simulate the H_2 adsorption on the substrates, a supercell of $4 \times 4 \times 1$ was used and the Brillouin zone was sampled using Monkhorst-Pack[80] scheme with a k-point mesh density of $<0.03\ \pi$ Å^{-1}. In addition, the structural edges of rGO were saturated with hydrogen bonds. The convergence criteria for the total energy was set to 10^{-5} eV and the force was set to 0.02 eV Å^{-1}. The van der Waals interaction was adopted according to DFT-D3 dispersion correction strategy to take the effect of nonbonding forces into account.[81] The adsorption energy (E_{ads}) of H_2 on each monolayer was calculated by the following equation:

$$E_{ads} = E(\text{slab}/H_2) - E(\text{slab}) - E(H_2) \quad (1)$$

where E(slab/H_2), E(slab), and E(H_2) denote the total energies of H_2 adsorption on the slab, an isolated slab, and a single H_2 molecule in the gas phase, respectively. The negative E_{ads} suggests the adsorption of H_2 is exothermic, while the positive value manifests the endothermic process of H_2. The optimized adsorption configurations and adsorption energies of H_2 on these surfaces are given in Figure 5c, where lower E_{ads} values mean stronger binding of H_2 to the substrates.

Supporting Information

Supporting Information is available from the Wiley Online Library or from the author.

Acknowledgements

The authors gratefully acknowledge the financial support from the National Natural Science Foundation of China (NSFC, 52372050), the Central Guidance for Local Science and Technology Development Funds Project (236Z4303G), the Hebei Natural Science Foundation (B2022408005), the Beijing-tianjin-hebei Basic Research Cooperation project (B2024408025), the Science and Technology Project of Hebei Education Department (JZX2023008, QN2022145), and the Key Research Projects of Higher Education Institutions of Henan Province (24A530009) and Special Fund for Young Teachers from the Zhengzhou University (JC23257011).

Conflict of Interest

The authors declare no conflict of interest.

Data Availability Statement

The data that support the findings of this study are available from the corresponding author upon reasonable request.

Keywords

graphene, hot/free electrons, hydrogen evolution, MXene, water splitting

Received: September 2, 2024
Revised: February 16, 2025
Published online:

[1] S. Y. Reece, J. A. Hamel, K. Sung, T. D. Jarvi, A. J. Esswein, J. J. Pijpers, D. G. Nocera, *Science* **2011**, *334*, 645.
[2] S. W. Kohl, L. Weiner, L. Schwartsburd, L. Konstantinovski, L. J. Shimon, Y. Ben-David, M. A. Iron, D. Milstein, *Science* **2009**, *324*, 74.
[3] M. Sayed, J. Yu, G. Liu, M. Jaroniec, *Chem. Rev.* **2022**, *122*, 10484.
[4] B. Qiu, M. Xing, J. Zhang, *Chem. Soc. Rev.* **2018**, *47*, 2165.
[5] M. Murdoch, G. Waterhouse, M. Nadeem, J. Metson, M. Keane, R. Howe, J. Llorca, H. Idriss, *Nat. Chem.* **2011**, *3*, 489.
[6] K. Maeda, K. Teramura, D. Lu, T. Takata, N. Saito, Y. Inoue, K. Domen, *Nature* **2006**, *440*, 295.
[7] L. Lin, Y. Ma, J. J. M. Vequizo, M. Nakabayashi, C. Gu, X. Tao, H. Yoshida, Y. Pihosh, Y. Nishina, A. Yamakata, N. Shibata, T. Hisatomi, T. Takata, K. Domen, *Nat. Commun.* **2024**, *15*, 397.
[8] P. She, J. Qin, J. Sheng, Y. Qi, H. Rui, W. Zhang, X. Ge, G. Lu, X. Song, H. Rao, *Small* **2022**, *18*, 2105114.
[9] C. Gao, T. Wei, Y. Zhang, X. Song, Y. Huan, H. Liu, M. Zhao, J. Yu, X. Chen, *Adv. Mater.* **2019**, *31*, 1806596.

[10] Y. Zhang, J. Qiu, B. Zhu, M. V. Fedin, B. Cheng, J. Yu, L. Zhang, *Chem. Eng. J.* **2022**, *444*, 136584.
[11] Y. Xiong, T. Liu, X. Wang, W. Liu, Y. Xue, X. Zhang, C. Xiong, J. Tian, *J. Alloys Compd.* **2022**, *918*, 165652.
[12] B. Xia, Y. Yang, Y. Zhang, Y. Xia, M. Jaroniec, J. Yu, J. Ran, S.-Z. Qiao, *Chem. Eng. J.* **2022**, *431*, 133944.
[13] B. Zhu, B. Cheng, J. Fan, W. Ho, J. Yu, *Small Struct.* **2021**, *2*, 2100086.
[14] W.-J. Ong, L.-L. Tan, Y. H. Ng, S.-T. Yong, S.-P. Chai, *Chem. Rev.* **2016**, *116*, 7159.
[15] C. Li, H. Xu, H. Xiong, S. Xia, X. Peng, F. Xu, X. Chen, *Adv. Funct. Mater.* **2024**, *34*, 2405539.
[16] Y. Q. Wang, Z. L. Qiao, H. Li, R. Zhang, Z. H. Xiang, D. P. Cao, S. T. Wang, *Angew. Chem., Int. Ed.* **2024**, *63*, 202404726.
[17] M. Wang, H. Lv, B. Dong, W. He, D. Yuan, X. Wang, R. Wang, *Angew. Chem., Int. Ed.* **2024**, *63*, 202401969.
[18] T. Hisatomi, K. Domen, *Nat. Catal.* **2019**, *2*, 387.
[19] G. Murali, J. K. Reddy Modigunta, Y. H. Park, J.-H. Lee, J. Rawal, S.-Y. Lee, I. In, S.-J. Park, *ACS Nano* **2022**, *16*, 13370.
[20] L. Zhang, J. Ran, S.-Z. Qiao, M. Jaroniec, *Chem. Soc. Rev.* **2019**, *48*, 5184.
[21] Y. Ma, Y. Li, F. Zhang, G. Hai, R. Wang, J. Liu, J. Bao, *Fuel* **2024**, *355*, 129413.
[22] L. K. Putri, B.-J. Ng, W.-J. Ong, H. W. Lee, W. S. Chang, S.-P. Chai, *ACS App. Mater. Inter.* **2017**, *9*, 4558.
[23] W. Yuan, L. Cheng, Y. An, S. Lv, H. Wu, X. Fan, Y. Zhang, X. Guo, J. Tang, *Adv. Sci.* **2018**, *5*, 1700870.
[24] X.-Q. Qiao, C. Li, W. Chen, H. Guo, D. Hou, B. Sun, Q. Han, C. Sun, D.-S. Li, *Chem. Eng. J.* **2024**, *490*, 151822.
[25] Y. Li, Z. Ren, Z. He, P. Ouyang, Y. Duan, W. Zhang, K. Lv, F. Dong, *Green Energy Environ.* **2024**, *9*, 623.
[26] E. Reisner, D. J. Powell, C. Cavazza, J. C. Fontecilla-Camps, F. A. Armstrong, *J. Am. Chem. Soc.* **2009**, *131*, 18457.
[27] Y. Sun, Y. Sun, X. Meng, Y. Gao, Y. Dall'Agnese, G. Chen, C. Dall'Agnese, X.-F. Wang, *Catal. Sci. Technol.* **2019**, *9*, 310.
[28] S. Zhang, L. Lu, J. Jiang, N. Liu, B. Zhao, M. Xu, P. Cheng, W. Shi, *Adv. Mater.* **2024**, *36*, 2403464.
[29] G. Murali, S. V. Prabhakar Vattikuti, Y. K. Kshetri, H. Lee, J. K. R. Modigunta, C. Seshendra Reddy, S. Park, S. Lee, B. Poornaprakash, H. Lee, Y. H. Park, J. Lee, S. Y. Park, I. In, *Chem. Eng. J.* **2021**, *421*, 129687.
[30] X. W. Ruan, X. Q. Cui, G. R. Jia, J. D. Wu, J. X. Zhao, D. J. Singh, Y. H. Liu, H. Y. Zhang, L. Zhang, W. T. Zheng, *Chem. Eng. J.* **2022**, *428*, 132579.
[31] C. Cheng, J. Zhang, B. Zhu, G. Liang, L. Zhang, J. Yu, *Angew. Chem., Int. Ed.* **2023**, *62*.
[32] Z. Liang, R. Shen, Y. H. Ng, P. Zhang, Q. Xiang, X. Li, *J. Mater. Sci. Technol.* **2020**, *56*, 89.
[33] D. Wang, X.-Q. Gong, *Nat. Commun.* **2021**, *12*, 158.
[34] X. Ruan, X. Cui, Y. Cui, X. Fan, Z. Li, T. Xie, K. Ba, G. Jia, H. Zhang, L. Zhang, W. Zhang, X. Zhao, J. Leng, S. Jin, D. J. Singh, W. Zheng, *Adv. Energy Mater.* **2022**, *12*, 2200298.
[35] J. Yang, D. Wang, H. Han, C. Li, *Acc. Chem. Res.* **2013**, *46*, 1900.
[36] D. Brida, A. Tomadin, C. Manzoni, Y. J. Kim, A. Lombardo, S. Milana, R. R. Nair, K. S. Novoselov, A. C. Ferrari, G. Cerullo, M. Polini, *Nat. Commun.* **2013**, *4*, 1987.
[37] Y. Wu, N. Yi, L. Huang, T. Zhang, S. Fang, H. Chang, N. Li, J. Oh, J. A. Lee, M. Kozlov, *Nat. Commun.* **2015**, *6*, 6141.
[38] T. Zhang, H. Chang, Y. Wu, P. Xiao, N. Yi, Y. Lu, Y. Ma, Y. Huang, K. Zhao, X.-Q. Yan, Z.-B. Liu, J.-G. Tian, Y. Chen, *Nat. Photon.* **2015**, *9*, 471.
[39] Y. Lu, Y. Yang, T. Zhang, Z. Ge, H. Chang, P. Xiao, Y. Xie, L. Hua, Q. Li, H. Li, B. Ma, N. Guan, Y. Ma, Y. Chen, *ACS Nano* **2016**, *10*, 10507.
[40] Y. Lu, B. Ma, Y. Yang, E. Huang, Z. Ge, T. Zhang, S. Zhang, L. Li, N. Guan, Y. Ma, Y. Chen, *Nano Res.* **2017**, *10*, 1662.
[41] S. Zhang, Y. Lu, X. Wan, Y. Duan, J. Gao, Z. Ge, L. Wei, Y. Chen, Y. Ma, Y. Chen, *RSC Adv.* **2020**, *10*, 42054.
[42] R. Xiao, C. Zhao, Z. Zou, Z. Chen, L. Tian, H. Xu, H. Tang, Q. Liu, Z. Lin, X. Yang, *Appl. Catal. B-Environ.* **2020**, *268*, 118382.
[43] X. Xie, N. Zhang, *Adv. Funct. Mater.* **2020**, *30*, 2002528.
[44] X. Li, Y. Bai, X. Shi, N. Su, G. Nie, R. Zhang, H. Nie, L. Ye, *Mater. Adv.* **2021**, *2*, 1570.
[45] Y. Li, L. Ding, S. Yin, Z. Liang, Y. Xue, X. Wang, H. Cui, J. Tian, *Nano-Micro Lett.* **2020**, *12*, 6.
[46] Y. Li, L. Ding, Z. Liang, Y. Xue, H. Cui, J. Tian, *Chem. Eng. J.* **2020**, *383*, 123178.
[47] T. Su, Z. D. Hood, M. Naguib, L. Bai, S. Luo, C. M. Rouleau, I. N. Ivanoy, H. Ji, Z. Qin, Z. Wu, *ACS Appl. Energy Mater.* **2019**, *2*, 4640.
[48] X. Xie, N. Zhang, Z.-R. Tang, M. Anpo, Y.-J. Xu, *Appl. Catal. B-Environ.* **2018**, *237*, 43.
[49] J. Ran, G. Gao, F.-T. Li, T.-Y. Ma, A. Du, S.-Z. Qiao, *Nat. Commun.* **2017**, *8*, 13907.
[50] X. Ruan, D. Meng, C. Huang, M. Xu, X. Wen, K. Ba, D. J. Singh, H. Zhang, L. Zhang, T. Xie, W. Zhang, W. Zheng, S. K. Ravi, X. Cui, *Small Methods* **2023**, *7*, 2300627.
[51] M. Naguib, M. Kurtoglu, V. Presser, J. Lu, J. Niu, M. Heon, L. Hultman, Y. Gogotsi, M. W. Barsoum, *Adv. Mater.* **2011**, *23*, 4248.
[52] Z. Ma, X. Zhou, W. Deng, D. Lei, Z. Liu, *ACS App. Mater. Inter.* **2018**, *10*, 3634.
[53] A. M. Navarro-Suárez, K. Maleski, T. Makaryan, J. Yan, B. Anasori, Y. Gogotsi, *Batteries Supercaps* **2018**, *1*, 33.
[54] J. Yan, C. E. Ren, K. Maleski, C. B. Hatter, B. Anasori, P. Urbankowski, A. Sarycheva, Y. Gogotsi, *Adv. Funct. Mater.* **2017**, *27*, 1701264.
[55] S. Xu, Y. Dall'Agnese, J. Li, Y. Gogotsi, W. Han, *Chem. - Eur. J.* **2018**, *24*, 18556.
[56] L. Xiu, Z. Wang, M. Yu, X. Wu, J. Qiu, *ACS Nano* **2018**, *12*, 8017.
[57] Y. Lu, S. Zhang, X. Han, X. Wan, J. Gao, C. Bai, Y. Li, Z. Ge, L. Wei, Y. Chen, Y. Ma, Y. Chen, *Nanotechnology* **2021**, *32*, 085401.
[58] Y. Sun, D. Jin, Y. Sun, X. Meng, Y. Gao, Y. Dall'Agnese, G. Chen, X.-F. Wang, *J. Mater. Chem. A.* **2018**, *6*, 9124.
[59] H. Dong, X. Zhang, Y. Zuo, N. Song, X. Xin, B. Zheng, J. Sun, G. Chen, C. Li, *Appl. Catal. A-Gen.* **2020**, *590*, 117367.
[60] C. Peng, P. Wei, X. Li, Y. Liu, Y. Cao, H. Wang, H. Yu, F. Peng, L. Zhang, B. Zhang, K. Lv, *Nano Energy* **2018**, *53*, 97.
[61] Y. Liu, Y.-H. Li, X. Li, Q. Zhang, H. Yu, X. Peng, F. Peng, *ACS Nano* **2020**, *14*, 14181.
[62] H. Xu, R. Xiao, J. Huang, Y. Jiang, C. Zhao, X. Yang, *Chinese J. Catal.* **2021**, *42*, 107.
[63] Y. Li, D. Zhang, X. Feng, Y. Liao, Q. Wen, Q. Xiang, *Nanoscale Adv.* **2019**, *1*, 1812.
[64] Y. Yang, D. Zhang, Q. Xiang, *Nanoscale* **2019**, *11*, 18797.
[65] K. Huang, C. Li, X. Zhang, L. Wang, W. Wang, X. Meng, *Green Energy Environ.* **2023**, *8*, 233.
[66] P. Tian, X. He, L. Zhao, W. Li, W. Fang, H. Chen, F. Zhang, Z. Huang, H. Wang, *Sol. Energy* **2019**, *188*, 750.
[67] Y.-H. Li, F. Zhang, Y. Chen, J.-Y. Li, Y.-J. Xu, *Green Chem.* **2020**, *22*, 163.
[68] Z. Ai, K. Zhang, B. Chang, Y. Shao, L. Zhang, Y. Wu, X. Hao, *Chem. Eng. J.* **2020**, *383*, 123130.
[69] Z. Yao, H. Sun, H. Sui, X. Liu, *Nanomaterials* **2020**, *10*, 452.
[70] J.-H. Zhao, L.-W. Liu, K. Li, T. Li, F.-T. Liu, *CrystEngComm.* **2019**, *21*, 2416.
[71] Y. Li, X. Deng, J. Tian, Z. Liang, H. Cui, *Appl. Mater. Today* **2018**, *13*, 217.
[72] L. Tie, S. Yang, C. Yu, H. Chen, Y. Liu, S. Dong, J. Sun, J. Sun, *J. Colloid Interface Sci.* **2019**, *545*, 63.
[73] J. Kang, S. Byun, S. Kim, J. Lee, M. Jung, H. Hwang, T. W. Kim, S. H. Song, D. Lee, *ACS Appl. Energy Mater.* **2020**, *3*, 9226.
[74] H. Wang, L. Chen, Y. Sun, J. Yu, Y. Zhao, X. Zhan, H. Shi, *Sep. Purif. Technol.* **2021**, *265*, 118516.

[75] M. Shao, Y. Shao, J. Chai, Y. Qu, M. Yang, Z. Wang, M. Yang, W. F. Ip, C. T. Kwok, X. Shi, Z. Lu, S. Wang, X. Wang, H. Pan, *J. Mater. Chem. A.* **2017**, *5*, 16748.
[76] M. Alhabeb, K. Maleski, B. Anasori, P. Lelyukh, L. Clark, S. Sin, Y. Gogotsi, *Chem. Mater.* **2017**, *29*, 7633.
[77] G. Kresse, J. Furthmüller, *Phys. Rev. B.* **1996**, *54*, 11169.
[78] P. E. Blöchl, *Phys. Rev. B.* **1994**, *50*, 17953.
[79] B. Hammer, L. B. Hansen, J. K. Nørskov, *Phys. Rev. B.* **1999**, *59*, 7413.
[80] H. J. Monkhorst, J. D. Pack, *Phys. Rev. B.* **1976**, *13*, 5188.
[81] S. Grimme, J. Antony, S. Ehrlich, H. Krieg, *J. Chem. Phys.* **2010**, *132*, 154104.